Reconstructing the dynamics of the outer electron radiation belt by means of the standard and ensemble Kalman filter with the VERB-3D code

Angelica Maria Castillo Tibocha[1], Jana de Wiljes[2], Yuri Y Shprits[3], and Nikita A Aseev[4]

[1]German Research Centre for Geosciences (GFZ)
[2]University of Potsdam, Institute of Mathematics
[3]Helmholtz Centre Potsdam
[4]GFZ German Research Centre for Geosciences

November 24, 2022

Abstract

Reconstruction and prediction of the state of the near-Earth space environment is important for anomaly analysis, development of empirical models and understanding of physical processes. Accurate reanalysis or predictions that account for uncertainties in the associated model and the observations, can be obtained by means of data assimilation. The ensemble Kalman filter (EnKF) is one of the most promising filtering tools for non-linear and high dimensional systems in the context of terrestrial weather prediction. In this study, we adapt traditional ensemble based filtering methods to perform data assimilation in the radiation belts. We use a one-dimensional radial diffusion model with a standard Kalman filter (KF) to assess the convergence of the EnKF. Furthermore, with the split-operator technique, we develop two new three-dimensional EnKF approaches for electron phase space density that account for radial and local processes, and allow for reconstruction of the full 3D radiation belt space. The capabilities and properties of the proposed filter approximations are verified using Van Allen Probe and GOES data. Additionally, we validate the two 3D split-operator Ensemble Kalman filters against the 3D split-operator KF. We show how the use of the split-operator technique allows us to include more physical processes in our simulations and offers computationally efficient data assimilation tools that deliver accurate approximations to the optimal solution of the KF and are suitable for real-time forecasting. Future applications of the EnKF to direct assimilation of fluxes and non-linear estimation of electron lifetimes are discussed.

Reconstructing the dynamics of the outer electron radiation belt by means of the standard and ensemble Kalman filter with the VERB-3D code

A. M. Castillo Tibocha[1,2*], **J. de Wiljes**[4], **Y. Y. Shprits**[1,2,3], **N. A. Aseev**[1,2]

[1]GFZ German Research Centre For Geosciences, Potsdam, Germany
[2]University of Potsdam, Institute of Physics and Astronomy, Potsdam, Germany
[3]Department of Earth, Planetary and Space Sciences, University of California, Los Angeles, CA, USA
[4]University of Potsdam, Institute of Mathematics, Potsdam, Germany

Key Points:

- We verify the convergence of the EnKF to the optimal state estimate given by KF.
- We develop, test, and successfully implement two new three-dimensional EnKF approaches that account for radial and local diffusion.
- We assimilate Van Allen Probes and GOES data, and compare different EnKF techniques in terms of the time evolution of PSD radial profiles.

*GFZ German Research Centre For Geosciences

Corresponding author: A. M. Castillo Tibocha, angelica@gfz-potsdam.de

Abstract

Reconstruction and prediction of the state of the near-Earth space environment is important for anomaly analysis, development of empirical models and understanding of physical processes. Accurate reanalysis or predictions that account for uncertainties in the associated model and the observations, can be obtained by means of data assimilation. The ensemble Kalman filter (EnKF) is one of the most promising filtering tools for non-linear and high dimensional systems in the context of terrestrial weather prediction. In this study, we adapt traditional ensemble based filtering methods to perform data assimilation in the radiation belts. We use a one-dimensional radial diffusion model with a standard Kalman filter (KF) to assess the convergence of the EnKF. Furthermore, with the split-operator technique, we develop two new three-dimensional EnKF approaches for electron phase space density that account for radial and local processes, and allow for reconstruction of the full 3D radiation belt space. The capabilities and properties of the proposed filter approximations are verified using Van Allen Probe and GOES data. Additionally, we validate the two 3D split-operator Ensemble Kalman filters against the 3D split-operator KF. We show how the use of the split-operator technique allows us to include more physical processes in our simulations and offers computationally efficient data assimilation tools that deliver accurate approximations to the optimal solution of the KF and are suitable for real-time forecasting. Future applications of the EnKF to direct assimilation of fluxes and non-linear estimation of electron lifetimes are discussed.

1 Introduction

Radiation belts electron dynamics exhibit strong changes in time and space during geomagnetically active periods over time scales ranging from minutes to hours. Enhanced radiation in space during geomagnetic storms can damage spacecraft electronics through deep dielectric and surface charging. Failure or damage of such systems yields significant societal and economical impacts. Therefore, understanding and prediction of particle dynamics in the near Earth has become increasingly important.

Several physics-based models that describe the evolution of electron phase space density in the radiation belt region have been developed (e.g. Salammbô (Beutier & Boscher, 1995; Bourdarie et al., 1996), DREAM-3D (Reeves et al., 2012), BAS (Glauert et al., 2014), VERB-3D code (Shprits, Subbotin, & Ni, 2009; Subbotin & Shprits, 2009). Physics-based models include uncertainties due to the errors in the initial and boundary conditions, wave models, transformation of fluxes from real space into invariant space, as well as potentially missing physical processes. Similarly, sparse observations are contaminated by secondary particles, noise and errors associated to spatial transformations. Therefore, the most reliable reconstruction and prediction of the state of the radiation belts can only be obtained by accounting for both, the data and the model, which is achieved through data assimilation.

The Kalman filter **(KF)** (Kalman, 1960) was developed in the context of engineering control problems and provides the *best linear unbiased estimator*, under the assumption of known Gaussian distributed model and observation errors. For non-linear systems, the sequential data assimilation algorithms most commonly used are the Extended Kalman filter (**EKF)** (Jazwinski, 1970), which entails a linearization of the model operator and the Ensemble Kalman filter **(EnKF)** (Evensen, 1994, 2003), which is a Monte Carlo approximation of the KF that does not require any linearization. The standard KF is a stable algorithm that offers the optimal estimate for single model runs of linear systems. However, one major advantage of the EnKF is the calculation of single error covariance matrices at every time step of the simulation. Since error estimation and assimilation of observations occur through the ensemble, the EnKF does not require linearization of neither the model nor the observation operators, allowing for non-linear effects to be taken into account.

The use of such data assimilation tools to analyse the state of the radiation belts is becoming increasingly popular. A variety of studies have used 1D radial diffusion models to apply the KF or the EKF algorithms, (e.g., Naehr & Toffoletto, 2005; Koller et al., 2005; Shprits et al., 2007; Kondrashov et al., 2007; Ni et al., 2009; Kondrashov et al., 2011; Daae et al., 2011; Shprits et al., 2012; Schiller et al., 2012), or the EnKF (e.g., Koller et al., 2007; Reeves et al., 2012; Godinez & Koller, 2012). Data assimilation in 1D space is useful to gain insights of the evolution of the system, but does not allow for propagation of covariances between different pitch angles and energies. Therefore, 1D approaches do not exploit the full potential of the satellite observations, and moreover, does not proper study of acceleration and loss processes. On the contrary, multidimensional models enable us to use the entire information on pitch angle distributions and energy spectra from different satellites.

Up until now, only two 3D data assimilation approaches for the radiation belt region have been implemented: one for the KF and one for the EnKF. Shprits et al. (2013) introduced the "operator-splitting" technique for 3D data assimilation with the KF. The authors showed the robustness of the 3D split-KF approach and presented the evolution of PSD radial profiles resulting from assimilation of CRRES data. More recently, Cervantes et al. (2020) presented simulations using a 3D split-KF tool, that includes mixed diffusion terms in the forecast step. Bourdarie and Maget (2012) used the EnKF to reconstruct radiation belts fluxes along satellite orbit, but they did not present global evolution of reconstructed fluxes and did not validate the EnKF against KF.

The goals of this work are: (1) to investigate the convergence of the state estimate from the EnKF to the optimal estimate from KF applied to a 1D radial diffusion model, and (2) to combine the operator-splitting and the EnKF approaches to obtain global reanalysis of the radiation belts. We address these goals as follows: we extend the split-operator technique to the EnKF in order to develop two computationally efficient 3D EnKF approximations. We use the VERB-3D code and the new split-EnKF methods to assimilate electron fluxes from Van Allen Probes and Geostationary Operational Environmental Satellites (GOES) in the entire 3D phase space. We present the global evolution of PSD in the radiation belts obtained with the new multidimensional EnKF approaches. Finally, we validate the convergence of our EnKF simulations by performing a systematic comparison of KF and EnKF methods for radiation belt electrons. Such a validation of data assimilation methods has not been provided in previous studies.

In the next Section, we describe the physics-based model and the satellite data. In Section 3, we present the theory of the filtering algorithms. Section 4 is devoted to the results of data assimilation experiments with real data. In Section 5, we discusse the results of the experiments and Section 6 gives an overview of the conclusions of this study and proposed future work.

2 VERB-3D model and Data

2.1 Model description

The 3D Versatile Electron Radiation Belt (VERB-3D) (Shprits, Subbotin, & Ni, 2009; Subbotin & Shprits, 2009) code solves the modified 3D Fokker-Planck equation that describes the time evolution of the phase-averaged electron phase space density (PSD or f) inside the Earth's magnetosphere in terms of the three adiabatic invariants (μ, J, Φ) (Schulz & Lanzerotti, 1974; Walt, 1994). Using bounce- and drift-averaged diffusion coefficients ($D_{L^*L^*}$, D_{pp}, $D_{p\alpha_0}$, $D_{\alpha_0 p}$, $D_{\alpha_0\alpha_0}$), this equation can be transformed into (L^*, p, α_0) coordinates and is known as the bounce- and drift-averaged Fokker-Planck-equation:

$$\frac{\partial f}{\partial t} = {L^*}^2 \left.\frac{\partial}{\partial L^*}\right|_{\mu,J} \left(\frac{1}{{L^*}^2} D_{L^*L^*} \left.\frac{\partial f}{\partial L^*}\right|_{\mu,J}\right) + \frac{1}{p^2} \left.\frac{\partial}{\partial p}\right|_{\alpha_0,L} \cdot p^2 \left(D_{pp} \left.\frac{\partial f}{\partial p}\right|_{\alpha_0,L} + D_{p\alpha_0} \left.\frac{\partial f}{\partial \alpha_0}\right|_{p,L}\right) +$$
$$\frac{1}{T(\alpha_0)\sin(2\alpha_0)} \left.\frac{\partial}{\partial \alpha_0}\right|_{p,L} \cdot T(\alpha_0)\sin(2\alpha_0) \left(D_{\alpha_0\alpha_0} \left.\frac{\partial f}{\partial \alpha_0}\right|_{p,L} + D_{\alpha_0 p} \left.\frac{\partial f}{\partial p}\right|_{\alpha_0,L}\right) + \frac{f}{\tau}, \tag{1}$$

where α_0 is the equatorial pitch angle, p is the relativistic momentum and $L^* = (2\pi M)/(\Phi R_E)$, with M the magnetic moment (Roederer & Zhang, 2014). $T(\alpha_0)$ is an approximation of the bounce frequency in a dipole field and is estimated after Lenchek et al. (1961). The radial diffusion coefficients ($D_{L^*L^*}$) are calculated following Brautigam and Albert (2000). Bounce-averaged diffusion coefficients are computed with the Full Diffusion Code (Shprits & Ni, 2009) using the hiss-wave parametrization of Orlova et al. (2014) and the chorus-wave (day and night side) parameterization of (Orlova & Shprits, 2014). The plasmapause location is estimated following Carpenter and Anderson (1992). The lifetime parameter τ is assumed to be infinite outside the loss cone and equal to a quarter of the electron bounce inside the loss cone.

The solution of equation (1) neglecting mixed diffusion can be computed on a grid with $25 \times 25 \times 25$ points along radial, energy, and pitch angle dimensions, with a uniform grid covering L^* values from 1 to 6.6. In order to obtain better resolution in high-PSD regions, e.g. at low energies and at the edge of the loss cone, logarithmic distributions are used for equatorial pitch angle grid points (from 0.3° to 89.7°) and energy grid points, which increase with decreasing L^*, i.e. at $L^* = 1$ the energy range is $2 - 200$ MeV and at $L^* = 6.6$ the energy range is $0.01 - 10$ MeV (Subbotin & Shprits, 2009; Subbotin et al., 2011). The initial PSD is calculated as the steady state solution of the radial diffusion equation. The six boundary conditions required to solve equation (1) are chosen as follows: at the inner radial boundary ($L^* = 1$), PSD is equal to zero to represent the losses to the atmosphere; at the upper radial boundary ($L^* = 6.6$), time-dependent PSD is estimated from GOES measurements. Setting PSD equal to zero at the lower pitch angle boundary ($\alpha_0 = 0.3°$), we account for electron precipitation in a weak diffusion regime (Shprits, Chen, & Thorne, 2009). A zero PSD-gradient is applied at the upper α-boundary ($\alpha_0 = 89.7°$) to describe a flat pitch angle distribution (Horne et al., 2003). At the upper energy boundary, a zero PSD boundary condition is applied representing the absence of high-energy electrons (> 10 MeV), while at the lower energy boundary PSD is set constant in time to represent a balance of convective source and loss processes.

2.2 Satellite Observations

We test the new split-operator EnKF techniques using electron observations obtained from the Van Allen Probes and GOES missions for the entire month of November, 2012. This particular period is chosen, as it includes both quiet and active geomagnetic conditions, and an intense storm (Kp = 6^+) on November 15.

The NASA's Van Allen Probes mission (formerly Radiation Belt Storm Probes (RBSP)), launched on 30.08.2012 from the Cape Canaveral, consisted of two spacecraft (probes A and B) at nearly identical highly elliptical orbits (HEO) with perigee of approximately 618 km, apogee of $\sim$ 30400 km ($\sim$ 5.8 Re geocentric) and 10° inclination (Mauk et al., 2012). The Energetic Particle, Composition and Thermal Plasma Suite (ECT) (Spence et al., 2013) on board both Van Allen Probes hosts four identical Magnetic Electron Ion Spectrometers (MagEIS) (Blake et al., 2013) and three Relativistic Electron Proton Telescopes (REPT) (Baker et al., 2012). These instruments provided pitch-angle resolved electron flux measurements from 01.09.2012 until 18.10.2019 covering large energy ranges: a) MagEIS: electron seed population to relativistic electron population ($20-240$ keV, $80-1200$ keV, $800-4800$ keV) and b) REPT: Very Energetic Electrons (2 MeV, 5 MeV, 10 MeV). In this study, we use MagEIS and REPT electron flux measurements from RBSP A and B averaged over 30min.

The GOES fleet are a series of meteorological geostationary satellites operated by the U.S. National Oceanic and Atmospheric Administration (NOAA) at nearly geosynchronous orbit (Data Book GOES, 2005). We use pitch-angle resolved electron flux measurements from the Magnetospheric Electron Detectors (MAGED) (Hanser, 2011; Rodriguez, 2014a) and the Energetic Proton, Electron, and Alpha Detectors (EPEAD) aboard GOES 13 and 15 (Rodriguez, 2014b). MAGED consists of nine solid-state-detector telescopes, five in the east-west (equatorial) plane and the other four in the north-south (meridional) plane, measuring electron fluxes at energies of: $30-50$ keV, $50-100$ keV, $100-200$ keV, $200-350$ keV and $350-600$ keV. In addition, onboard each GOES satellite two EPEADs, one detector oriented eastward and the other westward, measure MeV electron and proton flux data in two energy ranges: > 0.8 MeV and > 2 MeV. EPEAD integral fluxes and pitch-angles are obtained by averaging the measurements of the East and West telescopes. We use the $90°$ pitch-angle differential flux data from MAGED and fit the two integral channels of EPEAD to an exponential function. To obtain differential flux for energies of interest we use the exponential fits. In this study, we use electron flux observations from MAGED and EPEAD averaged over 30min intervals.

Measured electron fluxes (J) are converted to PSD (f) as: $f = J/p^2$ (Rossi & Olbert, 1970). Local magnetic field measurements are used to compute the first adiabatic invariant (μ). Using the IRBEM library (Boscher et al., 2013), we estimate the value of the second (K) and third adiabatic (L^*) invariants in the T89 magnetic field model (Tsyganenko, 1989).

3 Filtering Algorithms

In this section, the classic Kalman filter (Kalman, 1960) and the stochastic Ensemble Kalman filter (EnKF) (Evensen, 1994, 2003) are briefly reviewed, and their convergence and correspondence are discussed. We also give an overview of the split-operator adaptations of the KF and EnKF, and in subsection 3.5, we introduce our method of validation.

3.1 Kalman filter (KF)

Using VERB-3D and available satellite observations, our goal is to estimate the most probable state of the radiation belts (PSD at time k, denoted as $\mathbf{z}_k^a$) and the uncertainty of the state estimate (described by the error covariance matrix $\mathbf{P}_k^a$) associated with errors in the model and the data. Sequential data assimilation methods, such as the KF, allow us to determine estimates of the state and covariance analytically by defining an initial state vector $\mathbf{z}_0^a$ and initial covariance $\mathbf{P}_0^a$, and iterating over two elementary steps: 1) the *forecast step* and 2) the *analysis step.*

The ***forecast step:*** for a given linear dynamic represented by a set of partial differential equations, the time evolution of the state vector $\mathbf{z}$ is assumed to be governed by numerically discretized partial differential operator $\mathbf{M}$:

$$\mathbf{z}_k^f = \mathbf{M}\mathbf{z}_{k-1}^a, \tag{2}$$

where $\mathbf{M}$ is a linear discretization of equation (1) and $\mathbf{z}_k^f$ is the PSD state vector in the 3D phase space volume advanced by the model $\mathbf{M}$ in time, therefore superscripts "f" indicate here forecasted state. Deviations of the forecast state estimate from the true state of system are defined by the forecast error covariance matrix $\mathbf{P}_k^f$ which can be calculated from a previous analysis step as

$$\mathbf{P}_k^f = \mathbf{M}\mathbf{P}_{k-1}^a\mathbf{M}^T + \mathbf{Q}, \tag{3}$$

model errors are commonly assumed to be a sequence of uncorrelated white noise with zero mean and model error covariance $\mathbf{Q}$.

The ***analysis step or update step:*** the observations of the system $\mathbf{y}_k^{\text{obs}}$ are assumed to have uncertainties described by uncorrelated white noise with zero mean and observation error covariance $\mathbf{R}$. Combining the forecast error covariance matrix $\mathbf{P}_k^f$ with the uncertainty of the data $\mathbf{R}$, the Kalman filter finds optimal weights (defined in the Kalman gain $\mathbf{K}_k$) that minimize the error covariance $\mathbf{P}_k^a$ of the optimal state estimate $\mathbf{z}_k^a$ at time k,

$$\begin{aligned}\mathbf{K}_k &= \mathbf{P}_k^f\mathbf{H}^T(\mathbf{R} + \mathbf{H}\mathbf{P}_k^f\mathbf{H}^T)^{-1},\\ \mathbf{z}_k^a &= \mathbf{z}_k^f + \mathbf{K}_k(\mathbf{y}_k^{\text{obs}} - \mathbf{H}_k\mathbf{z}_k^f),\\ \mathbf{P}_k^a &= (\mathbf{I} - \mathbf{K}_k\mathbf{H})\mathbf{P}_k^f,\end{aligned} \tag{4}$$

the observation operator $\mathbf{H}$ maps the model space onto the observation space and accounts for differences in dimensionality between data and model, due to the sparsity of the observations. Note that the covariance update requires the model operator to be linear. For physical systems with underlying non-linear processes, this requirement does not hold in standard Kalman filter formulation and it is necessary to either linearize the equation for the covariance update, which is know in the literature as extended Kalman filter (Jazwinski, 1970) or to use an ensemble based update, such as in the Ensemble Kalman filter.

3.2 Ensemble Kalman filter (EnKF)

The EnKF can be interpreted as a purely statistical Monte Carlo approximation of the KF. In other words, the optimal state of the system $\mathbf{z}_k^a$ at time k is approximated by the mean $\overline{\mathbf{z}}_k^a$ of an ensemble of samples $\{\mathbf{z}_{i,k}^a\}$, where $i = 1, .., N_{\text{ens}}$:

$$\mathbf{z}_k^a \approx \overline{\mathbf{z}}_k^a = \frac{1}{N_{\text{ens}}}\sum_{i=1}^{N_{\text{ens}}} \mathbf{z}_{i,k}^a \tag{5}$$

the ensemble error covariance can then be interpreted as the error covariance of the optimal state estimate and gives the spread of the ensemble distribution. The error covariance matrices $\mathbf{P}_k^f$ and $\mathbf{P}_k^a$ are empirically approximated as

$$\begin{aligned}\mathbf{P}_e^f = \mathbf{P}_k^f &\approx \frac{1}{N_{\text{ens}} - 1}\left(\mathbf{z}_{i,k}^f - \overline{\mathbf{z}}_k^f\right)\left(\mathbf{z}_{i,k}^f - \overline{\mathbf{z}}_k^f\right)^T\\ \mathbf{P}_e^a = \mathbf{P}_k^a &\approx \frac{1}{N_{\text{ens}} - 1}\left(\mathbf{z}_{i,k}^a - \overline{\mathbf{z}}_k^a\right)\left(\mathbf{z}_{i,k}^a - \overline{\mathbf{z}}_k^a\right)^T\end{aligned} \tag{6}$$

Available observations $\mathbf{y}_k^{\text{obs}}$ are treated as random variables by generating an ensemble of observations. To this end, observation perturbations with $\epsilon_{i,k}$ are drawn from a Gaussian distribution with mean equal to the observed value and covariance R, which represents measurement errors:

$$\mathbf{y}_{i,k}^{\text{obs}} = \mathbf{y}_k^{\text{obs}} + \epsilon_{i,k} \tag{7}$$

where $i = 1, .., N_{\text{ens}}$. Every state in the ensemble is propagated in the update step, as follows:

$$\mathbf{z}_{i,k}^a = \mathbf{z}_{i,k}^f + \mathbf{K}_k\left(\mathbf{y}_{i,k}^{\text{obs}} - \mathbf{H}\mathbf{z}_{i,k}^f\right) \tag{8}$$

where the Kalman gain ($\mathbf{K}_k$) with the optimal weighting factors is calculated as in equation (4).

3.3 Convergence of the EnKF to the standard KF

It is important to note, that for a linear system and a large number of samples $N_{\text{ens}} \rightarrow \infty$ the EnKF and the KF produce the same mean and covariance estimate (Mandel et al., 2011). In other words, in the linear case the EnKF converges to the KF in the limit of an infinite number of ensemble members. Burgers et al. (1998) carefully revisited the analysis step of the KF and EnKF, and gave the fundamental setup of the EnKF for this convergence to hold. They showed that treating the observations as random variables allows the covariance of the analyzed ensemble $\mathbf{P}_e^a$ (in Eq. 6) to be expressed in the same way as in the analysis error covariance of the KF, i.e:

$$\mathbf{P}_e^a = (\mathbf{I} - \mathbf{K}_k\mathbf{H})\mathbf{P}_e^f + O(N^{-1/2}), \tag{9}$$

where fluctuations due to the finite ensemble size have on average zero mean and $O(N^{(-1/2)})$ rms magnitude. These deviations are proportional to $R - \overline{(\mathbf{y}_{i,k}^{\text{obs}} - \mathbf{y}_k^{\text{obs}})(\mathbf{y}_{i,k}^{\text{obs}} - \mathbf{y}_k^{\text{obs}})^T)}$ and $\overline{(\mathbf{z}_{i,k}^f - \mathbf{z}_k^f)(\mathbf{y}_{i,k}^{\text{obs}} - \mathbf{y}_k^{\text{obs}})^T})$. The authors state, that also in the forecast step correspondence between the KF and EnKF is given, when each ensemble member evolves according to:

$$\mathbf{z}_{i,k}^f = \mathbf{M}\mathbf{z}_{i,k-1}^a + d\mathbf{q}_i^k, \tag{10}$$

where $d\mathbf{q}_i^k$ is an stochastic forcing representing model errors from a distribution with zero mean and covariance $\mathbf{Q_e}$, defined as:

$$\mathbf{Q_e} = \overline{(d\mathbf{q}_i^k - \overline{d\mathbf{q}^k})(d\mathbf{q}_i^k - \overline{d\mathbf{q}^k})^T} = \overline{d\mathbf{q}^k(d\mathbf{q}^k)^T}. \tag{11}$$

In the limit of infinite ensemble size, convergence $\mathbf{Q_e} = \mathbf{Q}$ is given, $\mathbf{Q}$ being the model error covariance matrix of the KF. The ensemble mean then evolves as

$$\overline{\mathbf{z}_k^f} = \overline{\mathbf{M}(\mathbf{z}_{k-1}^f)} = \mathbf{M}(\overline{\mathbf{z}_{k-1}^f}) + \text{n.l} \tag{12}$$

where n.l represents possible non-linear terms in the model, that are not present in the standard KF. Thus, if the ensemble mean is used as the optimal state $\mathbf{z}^{a,f} = \overline{\mathbf{z}_{i,k}^{a,f}}$ and the EnKF is setup following equations (7), (10) and (11), the EnKF and the standard KF filter converge to the same state estimate in the linear case. For this reason, the EnKF is even used when non-linear effects are neglected and the underlying operator is indeed linear. For high dimensional problems, the optimal KF shows major shortcomings in terms of computational efficiency, as operating and storing large covariance matrices make the method very computationally demanding. In this regard, the EnKF has the advantage of using each error covariance matrix for the particular time step in question and then dismissing it.

It is crucial, however, that the use of the EnKF on finite ensemble sizes only provides an approximation of the KF, which makes this filtering method suboptimal. Despite the underlying Gaussian assumption, accuracy and stability have been rigorously shown for different approaches of the EnKF on non-linear operators (de Wiljes et al., 2018; de Wiljes & Tong, 2020).

3.4 Operator splitting technique

Shprits et al. (2013) proposed a suboptimal approximation of the KF that uses the operator-splitting method, often applied to solve partial differential equations. With this technique, the Kalman filter algorithm can be sequentially applied to the 1D diffusion operators in radial distance, energy and pitch-angle (mixed terms are neglected). Since each diffusion operates along one dimension in the model space, we can solve the equations sequentially for constant values of the other two dimensions, obtaining the solution in the entire 3D phase space (L^*, E, α). The update or analysis step of the KF is performed after each diffusion along one dimension. This "splitting" of the diffusions and thereby of the dimensionality of the problem allows the split-KF to operate with smaller matrices compared to the full-3D case and is, therefore, computationally much more convenient.

In this study, we use the split-operator method to separatly perform data assimilation using the EnKF for each diffusion operator. This method may be viewed as a form of localisation as correlations across dimensions are not considered anymore in the filter update. Computationally, the problem is reduced to the calculation of matrices in rather manageable sizes, i.e. the size of the state vector is always ($N_{ens} \times N$), where N is the number of grid nodes in the L, E or α dimensions, and N_{ens} is the number of ensembles. The $\mathbf{P}^f$ matrices are handled by the algorithm as 2D matrices of size ($N \times N$). Therefore, even for a large N_{ens}, the split-EnKF approach is, as in the split-KF approach, highly computationally efficient. For these reasons, the split-EnKF approach allows to increase dimensionality and also study different filter variations. We present two new split-EnKF variations and compare them with a 1D radial diffusion EnKF (e.g., Reeves et al., 2012), a 1D radial diffusion KF (e.g., Shprits et al., 2007) and the 3D split-operator KF (e.g., Shprits et al., 2013), as listed below:

1. In order to setup the EnKF and check its convergence to the KF, we implemented the EnKF in a simple 1D radial diffusion model, named here **EnKF(1D_RD)**, and compare the reanalysis results with a 1D-KF radial diffusion model, denoted **KF(1D_RD)** for simplicity.
2. We solve the three diffusion equations (radial, energy and pitch-angle) sequentially and assimilate data after calculation of each diffusion using a 1D split EnKF update, i.e. a total of three updates is performed. This filter approach is denoted here as **EnKF(3x1D)** and we compare its results to the KF analogous, which uses a standard KF for the 1D split update, for simplicity called **KF(3x1D)**. The pseudocode of this filter is given in Algorithm 1.
3. Here, we solve the three diffusion equations (radial, energy and pitch-angle), but we first assimilate data using a 1D split EnKF update after the radial diffusion part, and then use a 2D split EnKF update for the local diffusion, meaning that energy and pitch-angle diffusion are computed simultaneously. We denote this filter approach as **EnKF(1D_RD+2D_LD)** and present its pseudocode in Algorithm 2. A similar split-KF approach is rather computationally expensive, as it requires the calculation and storage of 4D forecast error covariance matrices every time step. Therefore, we compare the EnKF(1D_RD+2D_LD) with the **EnKF(3x1D)** and **EnKF(1D_RD)**.

3.5 Validation

In order to validate the results of our data assimilation experiments (see next section), we calculate the value of the innovation:

$$\mathbf{d} = \mathbf{y}_k^{\mathrm{obs}} - \mathbf{H}\mathbf{z}_k^f, \tag{13}$$

for every time step of the simulations. The value of $\mathbf{d}$ is the mathematical distance between the observations and the forecast vector. Additionally, the equations for the state estimate (Eq. (4) and (8)) reveal that $\mathbf{K}_k \cdot \mathbf{d} = (\mathbf{z}_k^a - \mathbf{z}_k^f)$. This means, that the innovation also gives a notion of the difference between the optimal state estimate and the forecast estimate. We use the innovation to quantify the accuracy of the state estimate obtained with a particular filter approach. The innovation becomes zero, when the estimate and the observations coincide. When the mean state underestimates the observations $\mathbf{d} > 0$ and the estimated state overestimates the observations $\mathbf{d} < 0$.

4 Reanalysis with satellite measurements

In this Section, we give a detailed description of the main setup of the EnKF split-operator variations and present the corresponding data assimilation results for satellite measurements for each proposed filter together with a systematic comparison with KF filtering results.

4.1 Setup of the EnKF(1D_RD)

As discussed in subsection 3.3, the state estimated with the EnKF converges to the optimal state estimated by the KF for linear systems and for a large number of ensemble members. For the initial setup and tests, we use a simple radial diffusion model with parametrized losses (Shprits et al., 2006). We first implement the standard Kalman filter assuming model and observation errors equal to 50%, and matrices $\mathbf{Q}$ and $\mathbf{R}$ are chosen to be diagonal matrices. The initial state $\mathbf{z}_0^a$ is estimated as a steady state solution of the radial diffusion equation. Then, using the setup of the KF(1D_RD) as a baseline,

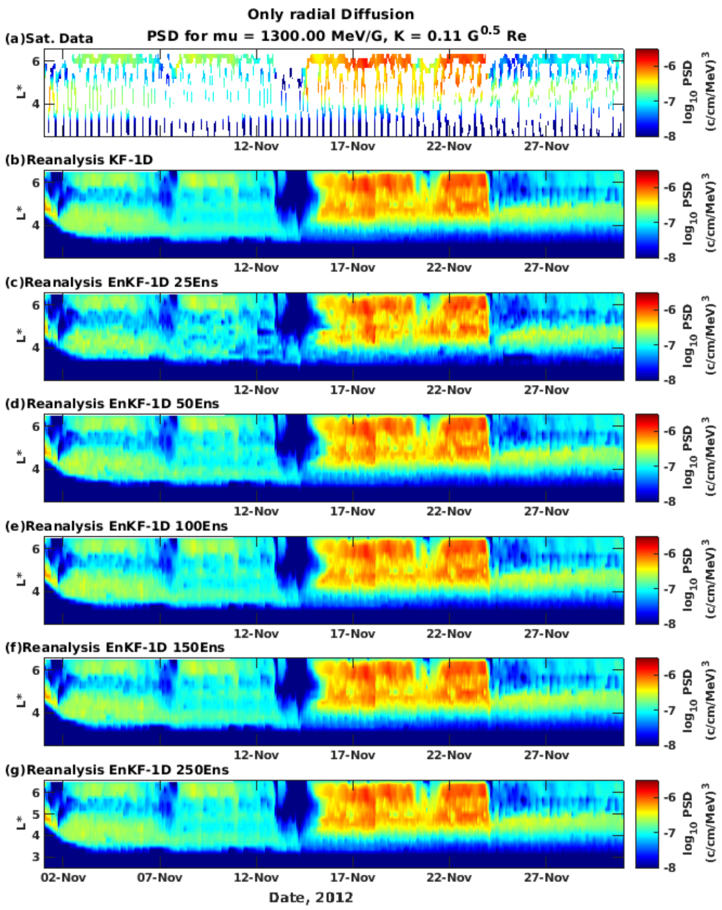

Figure 1. Simulation tests using filters KF(1D_RD) and EnKF(1D_RD): Electron PSD at $\mu = 1300$ MeV/G and $K = 0.11$ G$^{0.5}$ Re. a) Van Allen Probe and GOES observations, b) reanalysis results using KF(1D_RD), panels c) to g) reanalysis results using EnKF(1D_RD) for different number of ensembles, $N_{ens} = 25$, 50, 100, 150 and 250, respectively.

we implement the EnKF(1D_RD) as suggested by Burgers et al. (1998). The initial ensemble is constructed from the initial state of the KF(1D_RD) $\mathbf{z}_0^a$, by adding perturbations drawn from a Gaussian distribution with zero mean and variance of $0.5{\cdot}\mathbf{z}_0^a$. Similarly, the observation ensemble is created by adding Gaussian white noise with zero mean and variance of $0.5 \cdot \mathbf{y}_k^{\text{obs}}$ to each data point. The model error term, $d\mathbf{q}^k$, in equation (10), is modelled as a Gaussian distribution with zero mean and variance of $0.5{\cdot}\overline{\mathbf{z}_k^a}$. In order to determine the ensemble size, for which sufficient convergence is given, we run several test simulations using different number of ensembles and compare them with the KF(1D_RD) results. For our tests, satellite observations from Van Allen Probes and GOES from November 2012 are assimilated at a time step of 1 hour. The results of these test simulations are shown in Figure (1). In Panel a, the assimilated satellite observations are displayed, panel b shows the reanalysis results obtained using the KF(1D_RD), panels c to g present the reanalysis results obtained using the EnKF(1D_RD) for different number of ensembles, 25, 50, 100, 150 and 250, respectively. Visual inspection of the fig-

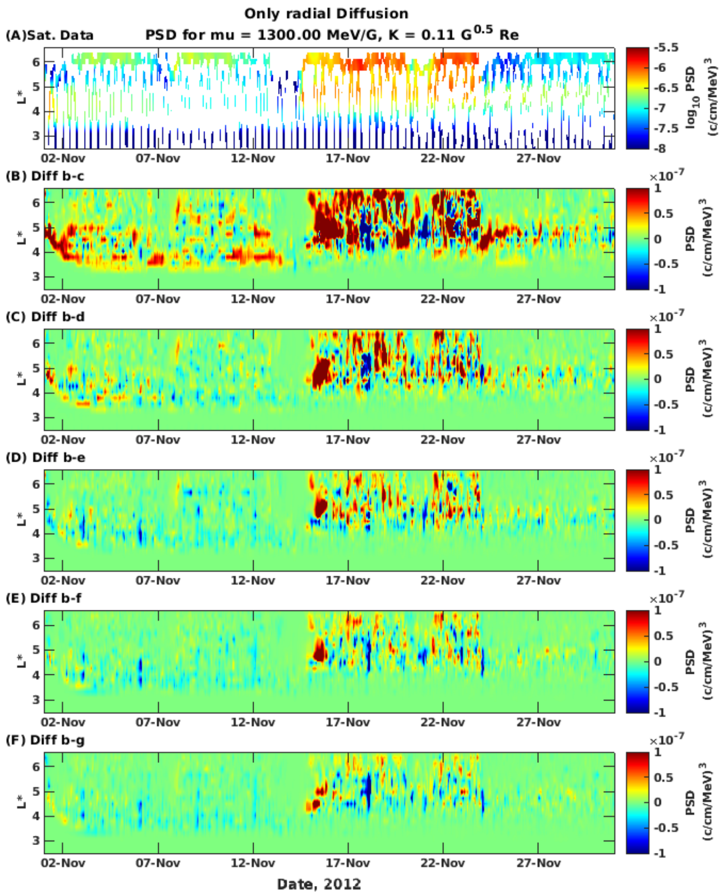

Figure 2. **Differences between simulation tests using filters KF(1D_RD) and EnKF(1D_RD):** Electron PSD at $\mu = 1300$ MeV/G and $K = 0.11$ G$^{0.5}$ Re. a) Van Allen Probe and GOES data, B) difference between panels b and c of Figure (1), C) difference between panels b and d of Figure (1), D) difference between panels b and e of Figure (1), E) difference between panels b and f of Figure (1), F) difference between panels b and g of Figure (1).

ure shows how the state of the radiation belts is improved by increasing the ensemble size. In order to assess when the EnKF(1D_RD) state estimate sufficiently approximates the KF(1D_RD) estimate, we calculate the difference of the PSD from KF(1D_RD) in panel b against PSD of EnKF(1D_RD) in panels c) to g). PSD differences are shown in Figure (2). Panel a depicts the satellite observations, panels B to F present the difference between panels $c{-}g$ and panel b of Figure (1), respectively. From panel B, it becomes clear that an ensemble size equal to the grid nodes in L-domain is too small and leads to poor results in the EnKF(1D_RD) estimate. Although, the values of the PSD difference clearly decrease with increasing number of ensembles, panels E and F are very similar, showing only larger deviations around November 16. Since, the simulation in panels f and g of Figure (1) were carried out using 150 and 250 ensemble members, the small differences in panels E and F of Figure (2) indicates that above 150 ensembles convergence to the KF(1D_RD) becomes so slow that an increase of 100 ensembles does not lead to significant improvement. For this reason, we consider ensembles with 150 members as sufficient to approximate the KF(1D_RD) and use this ensemble size for the data assimilation simulations presented in the next subsections.

4.2 Comparison between EnKF(1D_RD) and KF(1D_RD)

Now, that we estimated an adequate ensemble size, we can compare the reanalysis results obtained with the EnKF(1D_RD) and the KF(1D_RD). Figure (3, I) presents the electron PSD at $\mu = 1300$ MeV/G and $K = 0.11$ G$^{0.5}$ Re measured by the four satellites (panel a), the reanalysis results using EnKF(1D_RD)(panel b) and KF(1D_RD) (panel c), the difference between PSD both reanalysis, EnKF(1D_RD) - KF(1D_RD), (panel d) and the Kp index (bottom panel).

Noticeably, panels a), b) and c) reveals that both filters are able to reproduce the general features shown by the satellite observations throughout the simulated period. The difference between both simulations (panel d) allows for a more detailed overview of the filter performance. Blue tones in this plot indicate areas, where the EnKF(1D_RD) produces lower PSD values than the KF(1D_RD). Yellow to red colors indicate the opposite trend. The largest/lowest values in the PSD-difference are related to the recovery phase of the 15 November storm, when rather active geomagnetic conditions (see Kp, bottom panel) enhance electron PSD.

In order to assess the accuracy of the reanalysis in relation to the satellite data, we analyse the innovations of the two simulations. Resulting innovations for the two 1D_RD simulations are presented in Figure (3, II). The innovation of EnKF(1D_RD) is in panel a), the innovation of KF(1D_RD) in panel b), the difference between both innovations (EnKF(1D_RD) - KF(1D_RD)) is in panel c) and Kp is shown in the bottom panel.

Both innovation plots show very similar values and trends in time and radial distance. This indicates that the forecast state is corrected by a similar magnitude by both filters, i.e. similar difference to the observations. The highest innovation values are observed at the beginning of the simulation, at times of evident magnetopause crossings (8th and 15th Nov) and throughout $16-25$ November. This indicates that the model tends to underestimate PSD at these times so that the filter apply stronger corrections to the forecast. In panel c), some minor differences are observed mostly during $16-25$ November. Since the underlying model is the same for both filters, these differences can only arise from fluctuations in error covariance matrices of the EnKF caused by the use of a finite ensemble size (see Eq. 9). The plot in panel c, shows times and locations at which the EnKF(1D_RD) imposes larger (red) corrections on the forecast than the KF(1D_RD).

We analyse general trends in the innovation by calculating the mean innovation at $L^* > 3$ (main region of the outer belt) at every time step of the simulations. The mean innovations for the EnKF(1D_RD) reanalysis (black line) and for the KF(1D_RD) reanalysis (red dashed line) are displayed in panel four of Figure (3,II). Both curves show a very similar evolution in time, which is in agreement with panels a and b. Moreover, this figure nicely visualizes the variability of both innovations during the intense storm and active times (15 - 25. Nov). Interestingly, both innovations only vary within one order of PSD magnitude, being the only exception the major storm. In general, the EnKF(1D-RD) and the KF(1D-RD) filters produce very similar reanalysis results.

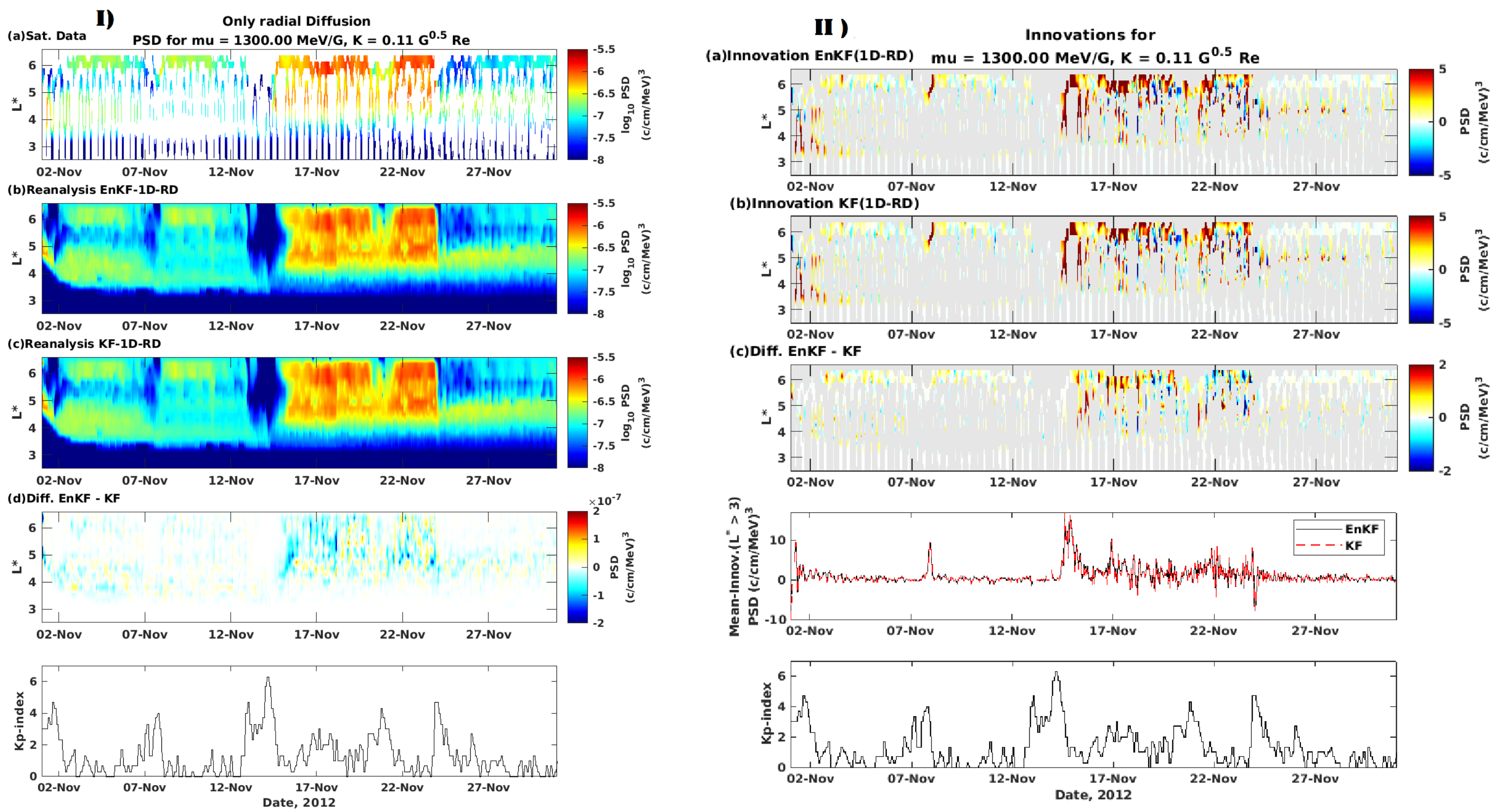

Figure 3. **Data assimilation results for EnKF(1D_RD) and KF(1D_RD) using Van Allen probes and GEOS observations from Nov. 2012:** Electron PSD at $\mu = 1300$ MeV/G and $K = 0.11$ G$^{0.5}$ Re. **I)** a) Van Allen Probe and GOES data, b) reanalysis results using EnKF(1D_RD), c) reanalysis results using KF(1D_RD), d) PSD difference between EnKF(1D_RD) and KF(1D_RD) reanalysis (EnKF - KF), bottom panel) Kp index. **II)** Innovation results for data assimilation using EnKF(1D_RD) and KF(1D_RD): Electron PSD at $\mu = 1300$ MeV/G and $K = 0.11$ G$^{0.5}$ Re. a) Innovation of EnKF(1D_RD) reanalysis, b) Innovation of KF(1D_RD) reanalysis, c) PSD difference between EnKF(1D_RD) and KF(1D_RD) innovations (EnKF - KF), d) Mean innovation (calculated at $L^* > 3$) for EnKF(1D_RD) (black line) and KF(1D_RD) (red dashed line), bottom panel) Kp index.

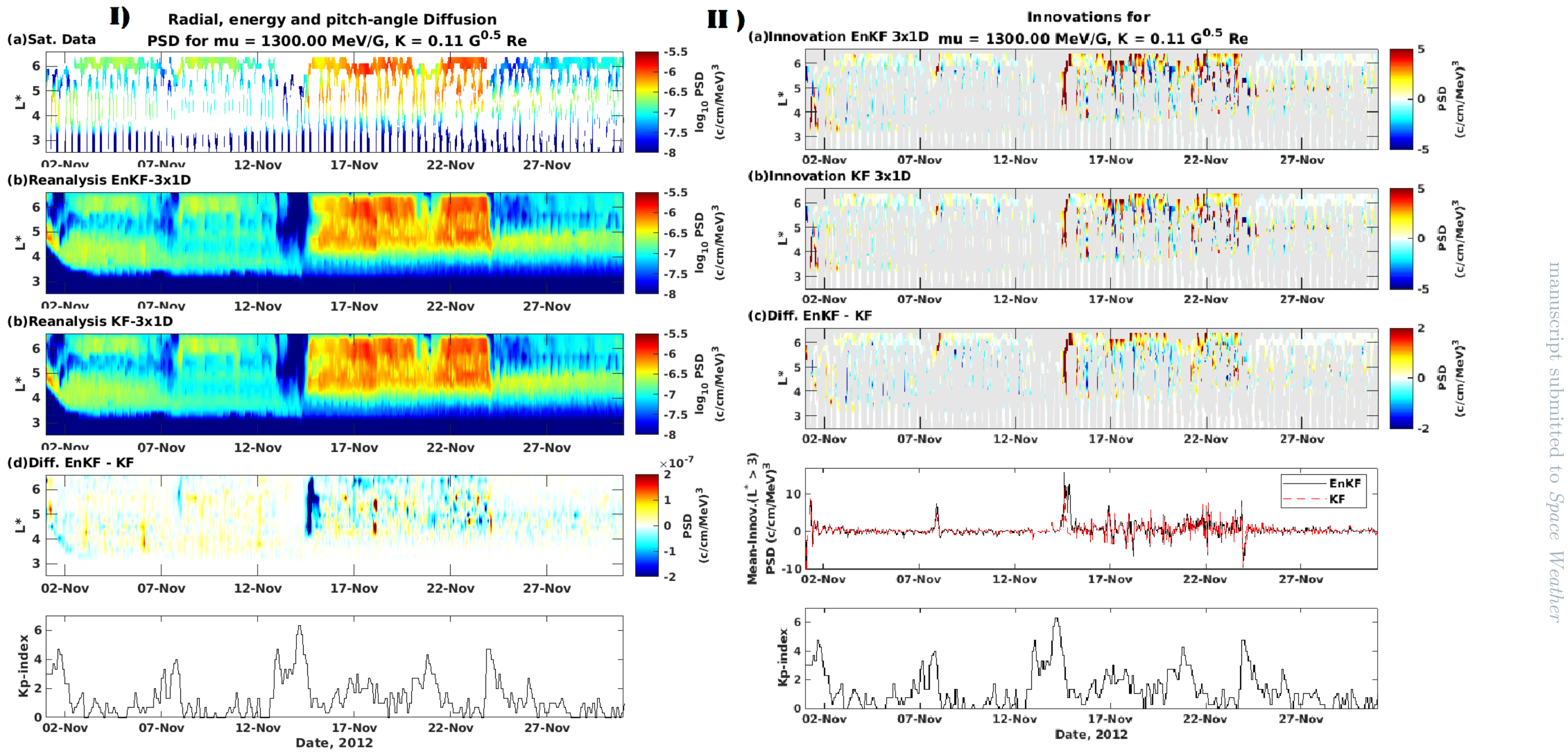

Figure 4. **Data assimilation results with EnKF(3x1D) and KF(3x1D) using Van Allen probes and GEOS observations from Nov. 2012: I)** Electron PSD at $\mu = 1300$ MeV/G and $K = 0.11$ G$^{0.5}$ Re. a) Van Allen Probes and GOES data, b) reanalysis results using EnKF(3x1D), c) reanalysis results using KF(3x1D), d) PSD difference between EnKF(3x1D) and KF(3x1D) reanalysis (EnKF(3x1D) - KF(3x1D)), bottom panel) Kp index. II) Innovation results for data assimilation with EnKF(3x1D) and KF(3x1D): Electron PSD at $\mu = 1300$ MeV/G and $K = 0.11$ G$^{0.5}$ Re. a) Innovation of EnKF(3x1D) reanalysis, b) Innovation of KF(3x1D) reanalysis, c) PSD difference between EnKF(3x1D) and KF(3x1D) innovations (EnKF(3x1D) - KF(3x1D)), d) Mean innovation (calculated for $L^* > 3$) for EnKF(3x1D) (black line) and KF(3x1D) (red dashed line), bottom panel) Kp index.

4.3 Reanalysis using the EnKF(3x1D) approach

In this section, we present our first split-operator variation of the EnKF, the **KF(3x1D)**. In this filtering approach, the radial, energy and pitch-angle diffusion equations are solved sequentially for the entire model space. After each diffusion a 1D update step takes place using a one-dimensional EnKF, as presented in EnKF(1D-RD). The model is thereby updated three times every time step. The convergence and performance of this 3D filter approach are tested using the same data assimilation setup presented in the previous sections and it is compared to its KF analogous filter approach (here denoted **KF(3x1D)**, suggested by Shprits et al. 2013.

Figure (4.I) shows the results of the EnKF(3x1D) data assimilation in the same format as Figure (3.I). Panel a) displays the assimilated Van Allen Probes and GOES measurements, panel b) presents the reanalysis performed with the EnKF(3x1D), panel c) shows the reanalysis of KF(3x1D) and panel d) illustrates the PSD-difference between both reanalysis (EnKF(3x1D) - KF(3x1D)). Similar to the EnKF(1D_RD), the overall PSD features observed in the satellite measurements are well reproduced by both 3D-split filters. However, differences in PSD between EnKF(3x1D) and KF(3x1D) are somewhat more pronounced than in the 1D-RD approach. During the first half of the simulation period, the EnKF(3x1D) tends to estimate higher PSD values than the KF(3x1D). For the second half of November, 2012, the trend appears to be reversed. On 15 November, when the intense storm causes the magnetopause to reach below $L^* \approx 4$, the difference between the simulations is largest. During the active period of $16-25$ November, the KF(3x1D) that produces larger PSD-values than the EnKF(3x1D).

Resulting innovations, displayed in Figure (4.II) for the EnKF(3x1D) reanalysis (panel a) and for the KF(3x1D) reanalysis (panel b) are overall very similar, but show smaller values for KF(3x1D) around November 15. The difference between both innovations (EnKF(3x1D) - KF(3x1D)) (in panel c) shows a trend toward negative values (blue colors) within the belt, particularly during 3 to 20 Nov. Since the underlying model is the same for both filters, this indicates that PSD estimated with KF(3x1D) is systematically closer to the data. There are two possible reasons for this: 1) the use of a finite number of ensembles will also lead to discrepancies in the estimation of the covariance matrices of EnKF and KF, and 2) error propagation due to sequential application of the update step (We will extend on this topic in the discussion section). The largest differences between innovations are observed around November 7 and on November 15, where EnKF(3x1D) reanalysis is more underestimated than the KF(3x1D) reanalysis. These features are also seen in the mean innovations above $L^* = 3$ (in panel four), which apart from those two times have pretty much the same evolution and variations, remaining generally within one order of magnitude. Overall, the EnKF(3x1D) and KF(3x1D) filters deliver a very similar reanalysis. It is important to note that the innovation of the 3D-split approaches is, in general, significantly smaller compared to 1D-RD filters. This means, this is related to the improved underlying physics-based model and to the repetition of the 1D update step.

4.4 Reanalysis using the EnKF(1D_RD+2D_LD) approach

Here, we present our second split-operator approach for the EnKF. In this filtering setup, the radial, energy and pitch-angle diffusion equations are solved sequentially for the entire model space. After the radial diffusion a 1D update step is performed in the L^*-dimension. In contrast to the 3x1D approach, after the calculation of local processes takes place, a single combined 2D update step in the energy and pitch-angle dimensions is performed. Therefore, the model is updated twice in this approximation. To test our 2D filter approach, we use the same data assimilation setup presented in the previous sections. Since a similar KF(1D_RD+2D_LD) filter approach is numerically highly complex and therefore very computationally expensive, we compare the EnKF(1D_RD+2D_LD) to a reanalysis performed with the EnKF(1D_RD) in this section, and to the results of EnKF(3x1D) in the next section.

Figure (5.I) shows the results of the EnKF(1D_RD+2D_LD) data assimilation in the same format as Figure (3.I). Panel b) displays the reanalysis performed with the EnKF (1D_RD+2D_LD), panel c) shows the reanalysis of EnKF(1D_RD) and panel d) illustrates the PSD-difference between both reanalysis (EnKF(1D_RD+2D_LD) - EnKF(1D_RD)). Both reanalysis present very similar trends overall and reproduce the main trends in the satellite data. The PSD-difference between the two filters is highest on 15 Nov. and during 16 - 25 Nov., where EnKF(1D_RD+2D_LD) produces slightly higher PSD values than EnKF(1D_RD). Interestingly, the fast losses observed on 15 November, caused by magnetopause compression, are reproduced slightly different in both filters.

Analysis of the innovations gives us detailed information about these features. Figure (5.II) presents the resulting innovations for the reanalysis with EnKF(1D_RD+2D_LD) (panel a) and with EnKF(1D_RD) (panel b). The difference between both innovations (EnKF(1D_RD+2D_LD) - EnKF(1D_RD)) is in panel c), mean innovations above $L^* = 3$ are in panel four and Kp is shown in the bottom panel. The innovation plots have similar features in time and space for both simulations. The innovation difference shows a tendency towards negative values (blue colors). In this case, the underlying models are different, therefore, the observed trend indicates a systematic overestimation of PSD in the 1D radial diffusion model. This is expected as the model on which EnKF(1D_RD+2D_LD) operates accounts for radial and local processes, being therefore more accurate. The mean innovations of both simulations also follow very similar trends, but the EnKF(1D_RD) curve (red line) ocasionally exceeds the EnKF(1D_RD+2D_LD) curve (black line), particularly during the sencond half of the simulation period (e.g. November 16, 17, 24).

4.5 Comparison between EnKF(1D_RD+2D_LD) and EnKF(3x1D)

In this section, we discuss the analysis of our two split-EnKF approaches by comparing the EnKF(1D_RD+2D_LD) results with the reanalysis results of EnKF(3x1D). Since the obtained PSD and innovations of both EnKF variations have already been presented, we only show their difference here. In Figure (6), panel b) displays the PSD difference between EnKF(1D_RD+2D_LD) and EnKF(3x1D) reanalysis, panel c) shows the difference between the innovations of both simulations, i.e. (EnKF(1D_RD+2D_LD) - EnKF(3x1D)), panel d) presents the mean innovation (for $L^* > 3$) for EnKF(1D_RD+2D_LD) (black line) and EnKF(3x1D) (red dashed line).

Although, both simulations converge to very similar solutions, the PSD differences reveal quite a few deviations. Particularly, large differences after the 15 November are observed. A general trend towards negative numbers in panel b, indicates that the state estimates of EnKF(3x1D) have larger values than those of EnKF(1D_RD+2D_LD). The innovation difference shows only a few large values at the beginning of the simulation and during 15−25 November. Red and yellow areas in the figure indicate that the innovation of the EnKF(1D_RD+2D_LD) has generally higher values than EnKF(3x1D). This is also observed in the mean innovations, especially around November 16. In this particular case, the physical models should be theoretically the same. However, due to the different implementation of the EnKF in the two approaches, more so the total updates performed in each filter approach, the underlying models become different. The EnKF(1D_RD+2D_LD) updates the model twice and the second update occurs in energy and pitch-angle diffusion simultaneously, involving covariance matrices of sizes ($N^2 \times N^2$). This means, that spurious correlations present in the covariances will certainly lead to differences in the estimates of EnKF(1D_RD+2D_LD) compared to those of EnKF(3x1D). Error propagation will also play a role for these two filtering approaches, but its effect on EnKF(1D_RD+2D_LD) results could have a rather small impact.

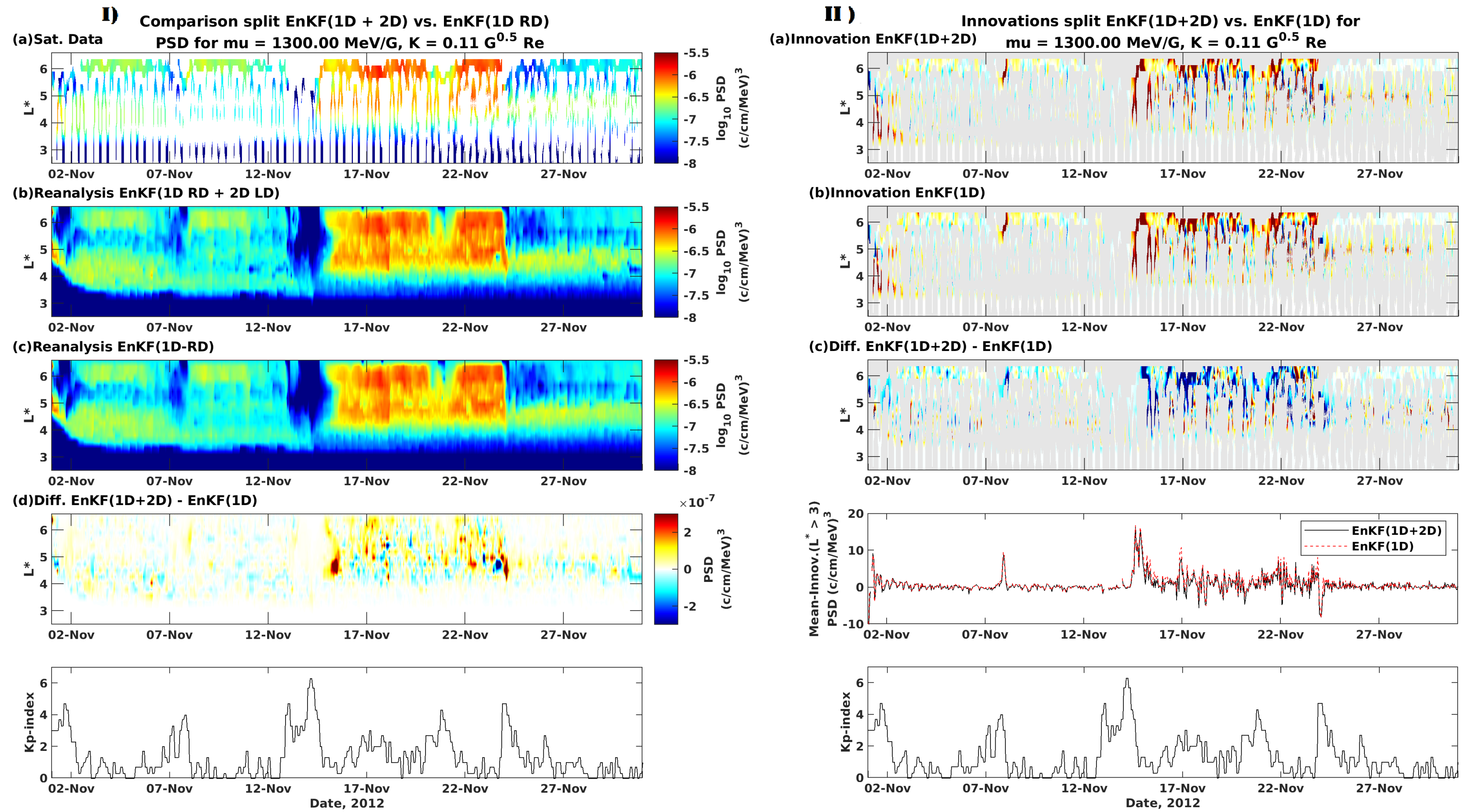

Figure 5. **Data assimilation results with EnKF(1D_RD+2D_LD) and EnKF(1D_RD) using Van Allen probes and GEOS observations from Nov. 2012:: I)** Electron PSD at $\mu = 1300$ MeV/G and $K = 0.11$ G$^{0.5}$ Re. a) Van Allen Probes and GOES data, b) reanalysis results using EnKF(1D_RD+2D_LD), c) reanalysis results using EnKF(1D_RD), d) PSD difference between EnKF(1D_RD+2D_LD) and EnKF(1D_RD) reanalysis (EnKF(1D_RD+2D_LD) - EnKF(1D_RD)), bottom panel) Kp index. **II)** Innovation results for data assimilation with EnKF(1D_RD+2D_LD) and EnKF(1D_RD): Electron PSD at $\mu = 1300$ MeV/G and $K = 0.11$ G$^{0.5}$ Re. a) Innovation of EnKF(1D_RD+2D_LD) reanalysis, b) Innovation of EnKF(1D_RD) reanalysis, c) PSD difference between EnKF(1D_RD+2D_LD) and EnKF(1D_RD) innovations (EnKF(1D_RD+2D_LD) - EnKF(1D_RD)), d) Mean innovation (calculated for $L^* > 3$) for EnKF(1D_RD+2D_LD) (black line) and EnKF(1D_RD) (red dashed line), bottom panel) Kp index.

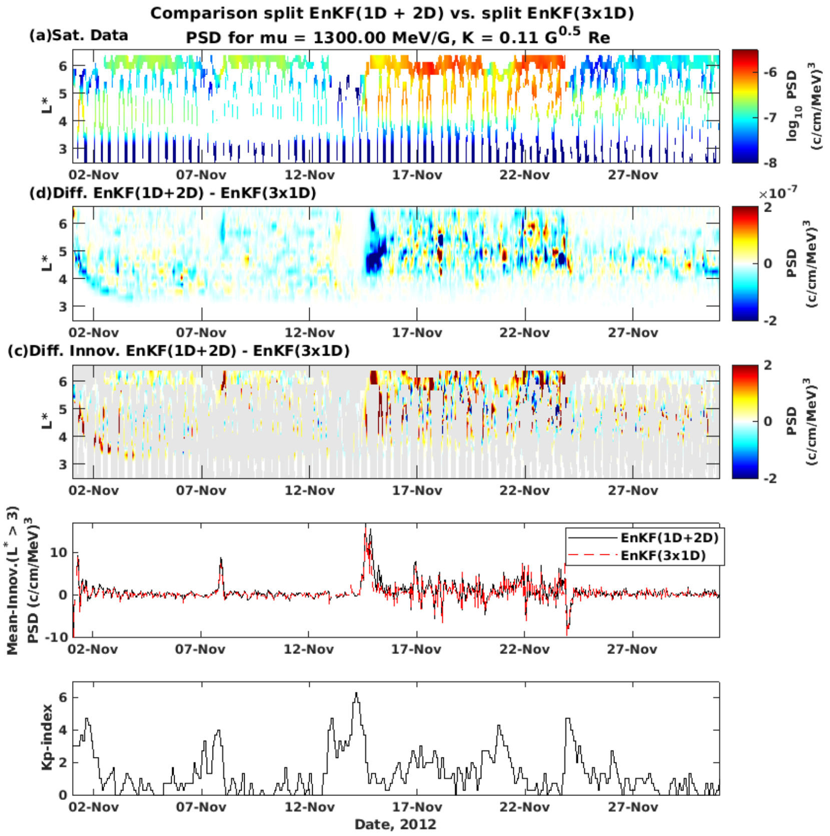

Figure 6. Data assimilation results with 1D_RD+2D_LD EnKF and EnKF(3x1D) using Van Allen probes and GEOS observations from Nov. 2012: Electron PSD at $\mu = 1300$ MeV/G and $K = 0.11$ G$^{0.5}$ Re. a) Van Allen Probes and GOES data, b) PSD difference between 1D_RD+2D_LD EnKF and EnKF(3x1D) reanalysis (1D_RD+2D_LD EnKF - EnKF(3x1D)), c) PSD difference between 1D_RD+2D_LD EnKF and EnKF(3x1D) innovations (1D_RD+2D_LD EnKF - EnKF(3x1D)), d) Mean innovation (calculated for $L^* > 3$) for 1D_RD+2D_LD EnKF (black line) and EnKF(3x1D) (red dashed line), bottom panel) Kp index.

5 Discussion

In this study, we developed and implemented two new split-operator approximations of the three dimensional EnKF to perform ensemble data assimilation of electron PSD in the radiation belts. Using a 1D radial diffusion model, we studied the convergence of the **EnKF(1D_RD)** to the optimal state of the system (**KF(1D_RD)**). Comparison between the reanalyses from both 1D filters showed that 150 ensemble members are sufficient to properly approximate the KF. Differences between the EnKF(1D_RD) approximation and the optimal KF(1D_RD) are rather negligible.

Implementation of the KF and the EnKF for high dimensional problems is computationally expensive. Using the initial setup for the EnKF(1D_RD), we implemented the more split-operator EnKF approaches of higher dimensionality and modeled the global state of the outer radiation belt for the month of November, 2012. We presented detailed comparison of the split KF and EnKF filtering tools, in order to verify the accuracy of the EnKF approaches. Our results suggest that although the split KF and EnKF approaches are simple approximations of the optimal KF, they are able to reconstruct accurately the radiation belt region. Only minor differences are observed at the beginning of the simulations, during active times and magnetopause compression events. This is consistent with the findings of Shprits et al. (2013) and justifies the general robustness of the split-EnKF approach.

In general, the simulations need about 3 days to level out discrepancies arising from the initial PSD. These initial errors appear to be larger in the 1D approaches, but become smaller for the (EnKF(3x1D) and EnKF(1D_RD+2D_LD)) methods. Additionally, the observed differences may be due to two facts: 1) Data assimilation requires mapping satellite observations onto invariant phase space coordinates (L^*, μ, K). However, L^* is a property of trapped particles. Therefore, no data points are available at higher L-shells during magnetopause compression events. Thus, filtering techniques cannot properly correct the PSD in those regions. 2) The EnKF may recognize spurious correlations that arise from the random perturbation of the observations, but are not really physical. This might be of particular importance for simulations with the EnKF(1D_RD + 2D_LD). Note that while it is true that the EnKF(1D_RD) filter converges to a reasonable solution, the reduction in the innovations of our two 3D EnKF approaches, EnKF(3x1D) and EnKF(1D_RD+2D_LD), indicates that the 3D update does allow for propagation of the satellite data to other energies and pitch angles. Therefore, a more accurate analysis is estimated, which in turn, leads to a better forecast estimate in the next time step.

A difficulty in dealing with the split-filters lays in the correct use of model errors. After application of the first analysis step, satellite data has been assimilated and thus improvement of the model is achieved. Therefore, for the second update step, the model errors described in matrix $\mathbf{Q}$ will not be the same as in the initial setup. A more accurate approach could, for instance, include some dynamical reduction of the model errors after each update iteration. This subject belongs to uncertainty estimation and lays beyond the scope of this study.

A major advantage of EnKF is that it does not require linearization of the model and observation operators. Therefore, non-linear effects can be accounted for using this tool. In future applications, we will use the split-EnKF approximations allows for direct assimilation of flux measurements by applying a nonlinear observation operator. Such an approach excludes errors due to re-mapping of fluxes into the model space, and will thereby reduce uncertainties in the analysis of the observation errors. Another field of application is the simultaneous non-linear estimation of the state and lifetimes of the system through state vector augmentation. This problem can be solved with the EnKF without the use of linear approximations. Similarly, the evaluation of model errors can be seen as a non-linear parameter estimation problem, which can be solved using the EnKF. Comparison of the free-forecasting qualities between the KF and the EnKF can now be performed. The understanding of the dynamical change in the model errors due to multiple update step application in the 3D split-approaches for KF and EnKF is important for optimal definition of the error statistics.

6 Conclusions

In this study, we setup, implement and validate two new split-operator approximations of the three dimensional EnKF, which allow us to reconstruct the entire state of the outer radiation belt. We provide a detailed comparison between different data assimilation tools using satellite observations. The main conclusions from our study are summarized below:

- Initial setup of the EnKF using the KF implementation on a simple 1D radial diffusion model allows us to find that 150 ensembles are sufficient to accurately model the optimal state solution of the KF.
- The use of the split-operator technique allows us to increase dimensionality in our simulations and tackles the issue of computational efficiency, which becomes particularly important at higher dimensions. Therefore, the new 3D split-EnKF approaches are suitable for forecasting purposes in real-time.
- Our validation method suggests that the split KF and EnKF methods show similar results. The use of the new 3D approaches reduces the global innovations in

comparison to 1D filters. This is partly due to the more accurate model but also due propagation of pitch angle and energy data into the model space, which yields an analysis state that is closer to the data. The use of this state estimate as initial condition in next step leads to a more accurate forecast state.

The **KF(3x1D)**, **EnKF (1D_RD+2D_LD)** and **EnKF(3D_RD)** tools are state of the art data assimilation techniques that reconstruct accurately the radiation belt region. The data assimilation tools developed in this study can be applied in the future to a variety of problems, including non-linear parameter estimation, non-linear assimilation of observations, free-prediction studies, error estimation and more.

Acknowledgments
The authors are grateful to the RBSP-ECT team for the provision of Van Allen Probes observations. We also thank the developers of the IRBEM library, which was adapted for use in the current study. We would like to thank Adam Kellermann and Sebastian Cervantes for instructing us on some the codes. We also thank Sebastian Reich for useful advise and discussions. The authors would like to thank the anonymous reviewers for their insightful comments. This research has been partially funded by Deutsche Forschungsgemeinschaft (DFG) - SFB1294/1 - 318763901 Project (B06) Novel methods for the 3D reconstruction of the dynamic evolution of the Van Allen belts using multiple satellite measurements. Jana de Wiljes was also supported by ERC Advanced Grant "ACRCC" (grant 339390) and by the Simons CRM Scholar-in-Residence Program.

Open Research

Data Availability Statement

The data used for this study is publicly available. The Kp index was provided by GFZ Potsdam (`https://www.gfz-potsdam.de/kp-index/`). All RBSP-ECT data are publicly available on the website: `http://www.RBSP-ect.lanl.gov/`. GOES electron data can also be accessed online at `https://satdat.ngdc.noaa.gov/sem/goes/data/full/`. The IRBEM library can be found under: `http://irbem.sourceforge.net`.

7 Appendix

In this section, we provide the reader with pseudo-codes for the algorithms of EnKF(3x1D) and EnKF(1D_RD+2D_LD). Implementation of the EnKF has been performed as suggested by (Evensen, 2003), in Section 4.3.1.

Algorithm 1 Split 3x1D Ensemble Kalman Filter (EnKF(3x1D))

1: Set variables initial mean $\mathbf{m}_0$ and covariance $\mathbf{P}_0$ and ensemble members N_{ens}

2: Initialise ensemble of particles $\mathbf{z}^a_{i,0} := \mathbf{z}^{a_{L\alpha p}}_{i,0} \sim N(\mathbf{m}_0, \mathbf{P}_0)$ with $i \in \{1, \ldots, N_{\text{ens}}\}$

3: **for** $k = 1 : T$ **do**

4: **1) Forecast and Analysis step radial distance L:** for all i

$$\begin{aligned}
\mathbf{z}^{f_L}_{i,k} &= \mathbf{M}_L\Big(\mathbf{z}^{a_{L\alpha p}}_{i,k-1}\Big)\\
\mathbf{z}^{a_L}_{i,k} &= \mathbf{z}^{f_L}_{i,k} - \mathbf{K}\Big(\mathbf{H}_L\mathbf{z}^{f_L}_{i,k} - \mathbf{y}^{\text{obs}}_k + \xi^L_{i,k}\Big)\\
\mathbf{K} &= \hat{\mathbf{P}}^{f_L}_k\mathbf{H}_L^\top(\mathbf{H}_L\hat{\mathbf{P}}^{f_L}_k\mathbf{H}_L^\top + \mathbf{R})^{-1}
\end{aligned}$$

5: **2) Forecast and Analysis step pitch angle α:**

$$\begin{aligned}
\mathbf{z}^{f_{L\alpha}}_{i,k} &= \mathbf{M}_\alpha\Big(\mathbf{z}^{a_L}_{i,k}\Big)\\
\mathbf{z}^{a_{L\alpha}}_{i,k} &= \mathbf{z}^{f_{L\alpha}}_{i,k} - \mathbf{K}\Big(\mathbf{H}_\alpha\mathbf{f}^{f_{L\alpha}} - \mathbf{y}^{\text{obs}}_k + \xi^\alpha_{i,k}\Big)\\
\mathbf{K} &= \hat{\mathbf{P}}^{f_{L\alpha}}_k\mathbf{H}_\alpha^\top(\mathbf{H}_\alpha\hat{\mathbf{P}}^{f_{L\alpha}}_k\mathbf{H}_\alpha^\top + \mathbf{R})^{-1}
\end{aligned}$$

6: **3) Forecast and Analysis step energy p:**

$$\begin{aligned}
\mathbf{z}^{f_{L\alpha p}}_i(\tau_n) &= \mathbf{M}_p\Big(\mathbf{z}^{a_{L\alpha}}_{i,k}\Big)\\
\mathbf{z}^{a_{L\alpha p}}_i(\tau_n) &= \mathbf{z}^{f_{L\alpha p}}_{i,k} - \mathbf{K}\Big(\mathbf{H}_p\mathbf{z}^{f_{L\alpha p}} - \mathbf{y}^{\text{obs}}_k + \xi_{i,k}\Big)\\
\mathbf{K} &= \hat{\mathbf{P}}^{f_{L\alpha p}}_k\mathbf{H}_p^\top(\mathbf{H}_p\hat{\mathbf{P}}^{f_{L\alpha p}}_k\mathbf{H}_p^\top + \mathbf{R})^{-1}
\end{aligned}$$

7: **end for**

8: Return

$$\begin{aligned}
\hat{\mathbf{m}}^{a_{L\alpha p}}_k &= \sum_{i=1}^{N_{\text{ens}}}\mathbf{z}^{a_{L\alpha p}}_{i,k}\\
\hat{\mathbf{P}}^{a_{L\alpha p}}_k &= \sum_{i=1}^{N_{\text{ens}}}(\mathbf{z}^{a_{L\alpha p}}_{i,k} - \hat{\mathbf{m}}^{a_{L\alpha p}}_k)(\mathbf{z}^{a_{L\alpha p}}_{i,k} - \hat{\mathbf{m}}^{a_{L\alpha p}})^\top
\end{aligned}$$

Algorithm 2 Split 1D_RD+2D_LD Ensemble Kalman Filter

Set variables initial mean $\mathbf{m}_0$ and covariance $\mathbf{P}_0$ and ensemble members N_{ens}

Initialise ensemble of particles $\mathbf{z}^{a}_{i,0} := \mathbf{z}^{a_{L\alpha p}}_{i,0} \sim N(\mathbf{m}_0, \mathbf{P}_0)$ with $i \in \{1, \dots, N_{\text{ens}}\}$

for $k = 1 : T$ **do**

1) Forecast and Analysis step radial distance L: for all i

$$\begin{aligned}
\mathbf{z}^{f_L}_{i,k} &= \mathbf{M}_L\Big(\mathbf{z}^{a_{L\alpha p}}_{i,k-1}\Big)\\
\mathbf{z}^{a_L}_{i,k} &= \mathbf{z}^{f_L}_{i,k} - \mathbf{K}\Big(\mathbf{H}_L \mathbf{z}^{f_L}_{i,k} - \mathbf{y}^{\text{obs}}_k + \xi^L_{i,k}\Big)\\
\mathbf{K} &= \hat{\mathbf{P}}^{f_L}_k \mathbf{H}_L^\top (H \hat{\mathbf{P}}^{f_L}_k \mathbf{H}_L^\top + \mathbf{R})^{-1}
\end{aligned}$$

2) Forecast and Analysis step pitch angle α and energy p:

$$\begin{aligned}
\mathbf{z}^{f_{L\alpha p}}_{i}(\tau_n) &= \mathbf{M}_{\alpha p}\Big(\mathbf{z}^{a_L}_{i,k}\Big)\\
\mathbf{z}^{a_{L\alpha p}}_{i}(\tau_n) &= \mathbf{z}^{f_{L\alpha p}}_{i,k} - \mathbf{K}\Big(\mathbf{H}_{\alpha p} \mathbf{z}^{f_{L\alpha p}} - \mathbf{y}^{\text{obs}}_k + \xi_{i,k}\Big)\\
\mathbf{K} &= \hat{\mathbf{P}}^{f_{L\alpha p}}_k \mathbf{H}_{\alpha p}^\top (\mathbf{H}_{\alpha p} \hat{\mathbf{P}}^{f_{L\alpha p}}_k \mathbf{H}_{\alpha p}^\top + \mathbf{R})^{-1}
\end{aligned}$$

end for

Return

$$\begin{aligned}
\hat{\mathbf{m}}^{a_{L\alpha p}}_k &= \sum_{i=1}^{N_{\text{ens}}} \mathbf{z}^{a_{L\alpha p}}_{i,k}\\
\hat{\mathbf{P}}^{a_{L\alpha p}}_k &= \sum_{i=1}^{N_{\text{ens}}} (\mathbf{z}^{a_{L\alpha p}}_{i,k} - \hat{\mathbf{m}}^{a_{L\alpha p}}_k)(\mathbf{z}^{a_{L\alpha p}}_{i,k} - \hat{\mathbf{m}}^{a_{L\alpha p}})^\top
\end{aligned}$$

References

Baker, D., Kanekal, S., Hoxie, V., Batiste, S., Bolton, M., Li, X., ... others (2012). The Relativistic Electron-Proton Telescope (REPT) Instrument on Board the Radiation Belt Storm Probes (RBSP) Spacecraft: Characterization of Earth's Radiation Belt High-Energy Particle Populations. In *The van allen probes mission* (pp. 337–381). Boston, MA: Springer. doi: 10.1007/978-1-4899-7433-4_11

Beutier, T., & Boscher, D. (1995). A three-dimensional analysis of the electron radiation belt by the Salammbô code. *Journal of Geophysical Research: Space Physics*, *100*(A8), 14853-14861. doi: 10.1029/94JA03066

Blake, J., Carranza, P., Claudepierre, S., Clemmons, J., Crain, W., Dotan, Y., ... others (2013). The magnetic electron ion spectrometer (MagEIS) instruments aboard the radiation belt storm probes (RBSP) spacecraft. In *The van allen probes mission* (pp. 383–421). Boston, MA: Springer. doi: 10.1007/978-1-4899-7433-4_12

Boscher, D., Bourdarie, S., O'Brien, P., & Guild, T. (2013). *The International Radiation Belt Environment Modeling (IRBEM) library.*

Bourdarie, S., Boscher, D., Beutier, T., Sauvaud, J.-A., & Blanc, M. (1996). Magnetic storm modeling in the Earth's electron belt by the Salammbô code. *Journal of Geophysical Research: Space Physics*, *101*(A12), 27171-27176. doi: 10.1029/96JA02284

Bourdarie, S., & Maget, V. F. (2012). Electron radiation belt data assimilation with an ensemble Kalman filter relying on the Salammbô code. *Annales Geophysi-*

cae, *30*(6), 929–943. doi: 10.5194/angeo-30-929-2012

Brautigam, D., & Albert, J. (2000). Radial diffusion analysis of outer radiation belt electrons during the October 9, 1990, magnetic storm. *Journal of Geophysical Research: Space Physics*, *105*(A1), 291–309. doi: 10.1029/1999JA900344

Burgers, G., Jan van Leeuwen, P., & Evensen, G. (1998). Analysis scheme in the ensemble Kalman filter. *Monthly weather review*, *126*(6), 1719–1724. doi: 10.1175/1520-0493(1998)126⟨1719:ASITEK⟩2.0.CO;2

Carpenter, D., & Anderson, R. (1992). An ISEE/whistler model of equatorial electron density in the magnetosphere. *Journal of Geophysical Research: Space Physics*, *97*(A2), 1097–1108. doi: 10.1029/91JA01548

Cervantes, S., Shprits, Y. Y., Aseev, N. A., Drozdov, A. Y., Castillo, A., & Stolle, C. (2020). Identifying Radiation Belt Electron Source and Loss Processes by Assimilating Spacecraft Data in a Three-Dimensional Diffusion Model. *Journal of Geophysical Research: Space Physics*, *125*(1), e2019JA027514. doi: 10.1029/2019JA027514

Daae, M., Shprits, Y., Ni, B., Koller, J., Kondrashov, D., & Chen, Y. (2011). Reanalysis of radiation belt electron phase space density using various boundary conditions and loss models. *Advances in Space Research*, *48*(8), 1327 - 1334. doi: 10.1016/j.asr.2011.07.001"

Data Book GOES, N. (2005). *Data Book, Prepared for National Aeronautics and Space Administration Goddard Space Flight Center Greenbelt, Maryland 20771.* (Tech. Rep.). Maryland 20771: CDRL PM-1-1-03, Section 5, 5–6.

de Wiljes, J., Reich, S., & Stannat, W. (2018). Long-Time Stability and Accuracy of the Ensemble Kalman–Bucy Filter for Fully Observed Processes and Small Measurement Noise. *SIAM Journal on Applied Dynamical Systems*, *17*(2), 1152-1181. doi: 10.1137/17M1119056

de Wiljes, J., & Tong, X. T. (2020). Analysis of a localised nonlinear ensemble Kalman Bucy filter with complete and accurate observations. *Nonlinearity*, *33*(9), 4752–4782. doi: 10.1088/1361-6544/ab8d14

Evensen, G. (1994). Sequential data assimilation with a nonlinear quasi-geostrophic model using Monte Carlo methods to forecast error statistics. *Journal of Geophysical Research: Oceans*, *99*(C5), 10143-10162. doi: 10.1029/94JC00572

Evensen, G. (2003). The ensemble Kalman filter: Theoretical formulation and practical implementation. *Ocean dynamics*, *53*(4), 343–367. doi: 10.1007/s10236-003-0036-9

Glauert, S. A., Horne, R. B., & Meredith, N. P. (2014). Three-dimensional electron radiation belt simulations using the BAS Radiation Belt Model with new diffusion models for chorus, plasmaspheric hiss, and lightning-generated whistlers. *Journal of Geophysical Research: Space Physics*, *119*(1), 268-289. doi: 10.1002/2013JA019281

Godinez, H. C., & Koller, J. (2012). Localized adaptive inflation in ensemble data assimilation for a radiation belt model. *Space Weather*, *10*(8). doi: 10.1029/2012SW000767

Hanser, F. (2011). *EPS/HEPAD calibration and data handbook (Tech. Rep. GOESN-ENG-048D).* Carlisle, MA.

Horne, R. B., Meredith, N. P., Thorne, R. M., Heynderickx, D., Iles, R. H. A., & Anderson, R. R. (2003). Evolution of energetic electron pitch angle distributions during storm time electron acceleration to megaelectronvolt energies. *Journal of Geophysical Research: Space Physics*, *108*(A1), SMP 11-1-SMP 11-13. doi: 10.1029/2001JA009165

Jazwinski, A. (1970). *Stochastic processes and filtering theory.* New York: Academic Press.

Kalman, R. E. (1960). A New Approach to Linear Filtering and Prediction Problems. *Transaction of the ASME Journal of Basic Engineering*, 35–45.

Koller, J., Chen, Y., Reeves, G. D., Friedel, R. H. W., Cayton, T. E., & Vrugt,

J. A. (2007). Identifying the radiation belt source region by data assimilation. *Journal of Geophysical Research: Space Physics*, *112*(A6). doi: 10.1029/2006JA012196

Koller, J., Friedel, R., & Reeves, G. (2005). Radiation belt data assimilation and parameter estimation. *LANL Reports*, *LA-UR-05, 6700*.

Kondrashov, D., Ghil, M., & Shprits, Y. Y. (2011). Lognormal Kalman filter for assimilating phase space density data in the radiation belts. *Space Weather*, *9*(11). doi: 10.1029/2011SW000726

Kondrashov, D., Shprits, Y. Y., Ghil, M., & Thorne, R. (2007). A Kalman filter technique to estimate relativistic electron lifetimes in the outer radiation belt. *Journal of Geophysical Research: Space Physics*, *112*(A10). doi: 10.1029/2007JA012583

Lenchek, A., Singer, S., & Wentworth, R. (1961). Geomagnetically trapped electrons from cosmic ray albedo neutrons. *Journal of Geophysical Research*, *66*(12), 4027–4046. doi: 10.1029/JZ066i012p04027

Mandel, J., Cobb, L., & Beezley, J. D. (2011). On the convergence of the ensemble Kalman filter. *Applications of Mathematics*, *56*(6), 533–541. doi: 10.1007/s10492-011-0031-2

Mauk, B., Fox, N. J., Kanekal, S., Kessel, R., Sibeck, D., & Ukhorskiy, A. (2012). Science objectives and rationale for the Radiation Belt Storm Probes mission. In *The van allen probes mission* (pp. 3–27). Boston, MA: Springer. doi: 10.1007/978-1-4899-7433-4_2

Naehr, S. M., & Toffoletto, F. R. (2005). Radiation belt data assimilation with an extended Kalman filter. *Space Weather*, *3*(6). doi: 10.1029/2004SW000121

Ni, B., Shprits, Y. Y., Nagai, T., Thorne, R., Chen, Y., Kondrashov, D., & Kim, H.-j. (2009). Reanalyses of the radiation belt electron phase space density using nearly equatorial CRRES and polar-orbiting Akebono satellite observations. *Journal of Geophysical Research: Space Physics*, *114*(A5). doi: 10.1029/2008JA013933

Orlova, K., & Shprits, Y. Y. (2014). Model of lifetimes of the outer radiation belt electrons in a realistic magnetic field using realistic chorus wave parameters. *Journal of Geophysical Research: Space Physics*, *119*(2), 770-780. doi: 10.1002/2013JA019596

Orlova, K., Spasojevic, M., & Shprits, Y. Y. (2014). Activity-dependent global model of electron loss inside the plasmasphere. *Geophysical Research Letters*, *41*(11), 3744-3751. doi: 10.1002/2014GL060100

Reeves, G. D., Chen, Y., Cunningham, G. S., Friedel, R. W. H., Henderson, M. G., Jordanova, V. K., ... Zaharia, S. (2012). Dynamic Radiation Environment Assimilation Model: DREAM. *Space Weather*, *10*(3). doi: 10.1029/2011SW000729

Rodriguez, J. (2014a). *GOES 13–15 MAGE/PD pitch angles algorithm theoretical basis document, version 1.0. Boulder, CO: NOAA National Geophysical Data Center.*

Rodriguez, J. (2014b). GOES EPEAD science-quality electron fluxes algorithm theoretical basis document. *NOAA Nat. Geophys. Data Center*.

Roederer, J., & Zhang, H. (2014). *Dynamics of Magnetically Trapped Particles: Foundations of the Physics of Radiation Belts and Space Plasmas.* Berlin, Germany: Springer. doi: 10.1007/978-3-642-41530-2

Rossi, B. B., & Olbert, S. (1970). *Introduction to the physics of space.* New York, NY: McGraw-Hill.

Schiller, Q., Li, X., Koller, J., Godinez, H., & Turner, D. L. (2012). A parametric study of the source rate for outer radiation belt electrons using a Kalman filter. *Journal of Geophysical Research: Space Physics*, *117*(A9). doi: 10.1029/2012JA017779

Schulz, M., & Lanzerotti, L. J. (1974). *Particle Diffusion in the Radiation Belts*

(Vol. 7). Berlin, Germany: Springer. doi: 10.1007/978-3-642-65675-0

Shprits, Y. Y., Chen, L., & Thorne, R. M. (2009). Simulations of pitch angle scattering of relativistic electrons with MLT-dependent diffusion coefficients. *Journal of Geophysical Research: Space Physics*, *114*(A3). doi: 10.1029/2008JA013695

Shprits, Y. Y., Daae, M., & Ni, B. (2012). Statistical analysis of phase space density buildups and dropouts. *Journal of Geophysical Research: Space Physics*, *117*(A1). doi: 10.1029/2011JA016939

Shprits, Y. Y., Kellerman, A., Kondrashov, D., & Subbotin, D. (2013). Application of a new data operator-splitting data assimilation technique to the 3-D VERB diffusion code and CRRES measurements. *Geophysical Research Letters*, *40*(19), 4998-5002. doi: 10.1002/grl.50969

Shprits, Y. Y., Kondrashov, D., Chen, Y., Thorne, R., Ghil, M., Friedel, R., & Reeves, G. (2007). Reanalysis of relativistic radiation belt electron fluxes using CRRES satellite data, a radial diffusion model, and a Kalman filter. *Journal of Geophysical Research: Space Physics*, *112*(A12). doi: 10.1029/2007JA012579

Shprits, Y. Y., & Ni, B. (2009). Dependence of the quasi-linear scattering rates on the wave normal distribution of chorus waves. *Journal of Geophysical Research: Space Physics*, *114*(A11). doi: 10.1029/2009JA014223

Shprits, Y. Y., Subbotin, D., & Ni, B. (2009). Evolution of electron fluxes in the outer radiation belt computed with the VERB code. *Journal of Geophysical Research: Space Physics*, *114*(A11). doi: 10.1029/2008JA013784

Shprits, Y. Y., Thorne, R. M., Friedel, R., Reeves, G. D., Fennell, J., Baker, D. N., & Kanekal, S. G. (2006). Outward radial diffusion driven by losses at magnetopause. *Journal of Geophysical Research: Space Physics*, *111*(A11). doi: 10.1029/2006JA011657

Spence, H., Reeves, G., Baker, D., Blake, J., Bolton, M., Bourdarie, S., ... others (2013). Science Goals and Overview of the Radiation Belt Storm Probes (RBSP) Energetic Particle, Composition, and Thermal Plasma (ECT) Suite on NASA's Van Allen Probes Mission. In *The van allen probes mission* (pp. 311–336). Boston, MA: Springer. doi: 10.1007/978-1-4899-7433-4_10

Subbotin, D. A., & Shprits, Y. Y. (2009). Three-dimensional modeling of the radiation belts using the Versatile Electron Radiation Belt (VERB) code. *Space Weather*, *7*(10). doi: 10.1029/2008SW000452

Subbotin, D. A., Shprits, Y. Y., & Ni, B. (2011). Long-term radiation belt simulation with the VERB 3-D code: Comparison with CRRES observations. *Journal of Geophysical Research: Space Physics*, *116*(A12). doi: 10.1029/2011JA017019

Tsyganenko, N. (1989). A magnetospheric magnetic field model with a warped tail current sheet. *Planetary and Space Science*, *37*(1), 5 - 20. doi: 10.1016/0032-0633(89)90066-4

Walt, M. (1994). *Introduction to geomagnetically trapped radiation* (Vol. 10). Cambridge, UK: Cambridge University Press.